



# Zinc-assisted MgO template synthesis of porous carbon-supported Fe-N<sub>x</sub> sites for efficient oxygen reduction reaction catalysis in Zn-air batteries

Xiangyu Lu<sup>a</sup>, Hao Xu<sup>a</sup>, Peixia Yang<sup>a,\*</sup>, Lihui Xiao<sup>a</sup>, Yaqiang Li<sup>a</sup>, Jingyuan Ma<sup>b,\*</sup>, Ruopeng Li<sup>a</sup>, Lilai Liu<sup>c</sup>, Anmin Liu<sup>d</sup>, Veniamin Kondratiev<sup>e</sup>, Oleg Levin<sup>e</sup>, Jinqiu Zhang<sup>a</sup>, Maozhong An<sup>a</sup>

<sup>a</sup> MIIT Key Laboratory of Critical Materials Technology for New Energy Conversion and Storage, School of Chemistry and Chemical Engineering, Harbin Institute of Technology, Harbin 150001, China

<sup>b</sup> Shanghai Synchrotron Radiation Facility, Zhangjiang Laboratory (SSRF, ZJLab), Shanghai Advanced Research Institute, Chinese Academy of Sciences, Shanghai 201204, China

<sup>c</sup> College of Environmental and Chemical Engineering, Heilongjiang University of Science and Technology, Harbin 150022, China

<sup>d</sup> State Key Laboratory of Fine Chemicals, School of Chemical Engineering, Dalian University of Technology, Dalian 116086, China

<sup>e</sup> St. Petersburg State University, 7/9 Universitetskaya Nab., St. Petersburg 199034, Russian Federation

## ARTICLE INFO

### Keywords:

Atomically dispersed catalysts  
Oxygen reduction  
Fe-N<sub>4</sub> sites  
Porous structure  
Zn-air batteries

## ABSTRACT

Atomically dispersed iron-nitrogen-carbon catalysts offer great potential in oxygen reduction reaction (ORR), yet the poor exposure and low density of Fe-N<sub>x</sub> sites causes relatively low ORR activity. Herein, a zinc-assisted MgO template strategy is reported to construct porous carbon-supported Fe-N<sub>4</sub> sites (Fe-N-C). Iron atoms surrounded by zinc species are converted to abundant Fe-N<sub>4</sub> sites rather than Fe containing nanoparticles. Meanwhile, both the zinc species and the MgO template can effectively produce porous structure so as to increase the utilization of Fe-N<sub>4</sub> sites. Fe-N-C achieves superior ORR performance and stability in alkaline medium. Theoretical calculations manifest that Fe-N<sub>4</sub> sites can narrow the energy barrier for ORR. Moreover, finite element simulation exhibits the porous framework in Fe-N-C could significantly accelerate the diffusion of O<sub>2</sub>. Therefore, Fe-N-C provides a high peak power density and superior discharge ability toward Zn-air batteries.

## 1. Introduction

As eco-friendly energy devices, Zn-air batteries have acquired much attention. However, the use of these technologies is hampered by sluggish kinetics of ORR [1–3]. To date, platinum (Pt)-based catalysts are currently utilized as commercial ORR catalysts [4–6], but the wide application of them is limited by their expensive cost and insufficient durability [7,8]. Thus, it is significantly important to explore cost-effective, high-active, and stable Pt-free ORR catalysts [9–11].

Towards this goal, single Fe embedded in nitrogen-carbon catalysts (Fe/N-C) are explored as one of the most attractive Pt-free catalysts [12–15], in which the Fe-N<sub>x</sub> sites play a crucial role in ORR activity [16–19]. These Fe/N-C are typically obtained via pyrolysis of the precursors containing iron- and nitrogen -source [1,20,21]. Nevertheless, Fe atoms easily migrate and aggregate into relatively large Fe particles (e.g., metallic Fe nanoparticles, Fe<sub>3</sub>C, and Fe<sub>2</sub>O<sub>3</sub>) during pyrolysis, leading to a low density of atomic Fe-N<sub>x</sub> sites [22,23]. Therefore, the traditional preparation method does not give a satisfactory result with

respect to the abundant Fe-N<sub>x</sub> sites, thereby leading to unsatisfactory ORR activity. Moreover, bulk Fe-N<sub>x</sub> sites buried inside the carbon matrix are not easily accessible for oxygen molecules (O<sub>2</sub>), resulting in insufficient catalysts/electrolyte/O<sub>2</sub> three-phase boundary for ORR [24,25]. Consequently, the low density and poor exposure of Fe-N<sub>x</sub> sites greatly limits ORR activity for currently reported catalysts.

Therefore, the construction of highly porous matrix structure with easily accessible active sites is an excellent strategy to accelerate the diffusion of O<sub>2</sub> and penetration of electrolyte in porous channels, and thus effectively improve ORR performance [26–29]. In general, porous carbon is prepared by the hard template (e.g., silica) [30–32]. However, the producing process is complicated and environmentally unfriendly for removing the silica template as it requires corrosive HF or alkali solution [33]. Therefore, it is imperative to develop a rational method to achieve minimized agglomerates of Fe atom, abundant Fe-N<sub>x</sub> active sites, and porous framework.

Herein, a facile synthesis strategy based on the use of combined zinc and MgO template was proposed to prepare porous carbons with densely

\* Corresponding authors.

E-mail addresses: [yangpeixia@hit.edu.cn](mailto:yangpeixia@hit.edu.cn) (P. Yang), [majy@sari.ac.cn](mailto:majy@sari.ac.cn) (J. Ma).

<https://doi.org/10.1016/j.apcatb.2022.121454>

Received 17 December 2021; Received in revised form 28 March 2022; Accepted 25 April 2022

Available online 28 April 2022

0926-3373/© 2022 Elsevier B.V. All rights reserved.

exposed Fe-N<sub>4</sub> active sites. Fe atoms surrounded by Zn nodes can effectively convert to the atomically dispersed Fe-N<sub>4</sub> sites rather than Fe containing nanoparticles, thereby forming dense Fe-N<sub>4</sub> active sites. Meanwhile, a lot of Zn species can be evaporated, leading to abundant pore structure. Additionally, the MgO template could be easily removed via a mild acid solution, leaving mesopores and macropores, which can promote the diffusion of O<sub>2</sub> and the penetration of electrolyte. As a result, the integration of dense Fe-N<sub>4</sub> active sites with porous structure endow Fe-N-C with an exceptional ORR activity, surpassing Pt/C.

## 2. Experimental Section

### 2.1. Synthesis of catalysts

The particle size of MgO (CAS No. 1309–48–4) template is 40–60 nm from Macklin's specification sheet. In addition, the SEM was employed to directly observe the size of the MgO template particles. As shown in Fig. S1, the particle size of MgO is from 10 to 100 nm.

0.2 mmol of Fe(NO<sub>3</sub>)<sub>3</sub>·9 H<sub>2</sub>O, 4 mmol of Zn(NO<sub>3</sub>)<sub>2</sub>·6 H<sub>2</sub>O, and MgO (2 g) were dissolved in ultrapure water (25 mL), after which was stirred magnetically for 2 h. Thereafter, 1 g of polyvinyl pyrrolidone (PVP) was dissolved in the above solution, and stirred for 4 h. After being freeze-dried, the obtained sample was heated to 900 °C for 2 h (5 °C min<sup>-1</sup>) at H<sub>2</sub>/Ar-atmosphere. Fe-N-C was obtained by hydrochloric acid treatment.

### 2.2. Electrochemical measurements

Electrochemical tests were conducted in a CHI760E workstation by a three-electrode system. Hg/HgO (alkaline media) and Hg/Hg<sub>2</sub>SO<sub>4</sub> (acidic media) electrode were used as reference electrodes. Graphite sheet serve as counter electrode. A glassy-carbon electrode by the coating of catalyst-coated was used as the working electrode, whose diameter is 5 mm. The catalyst (5 mg) was dispersed into a solution (1000 μL), which consists isopropanol (640 μL), Nafion (40 μL), and ultrapure water (320 μL). Next, the catalyst ink (18 μL) and Pt/C (9 μL) were dropped onto on electrode.

The yield of hydrogen peroxide and number of electron transfers (n) were measured according to the following equations:

$$\text{H}_2\text{O}_2(100\%) = 200 \frac{I_{\text{R/N}}}{I_{\text{D}} + I_{\text{R/N}}} \quad (1)$$

$$n = 4 \frac{I_{\text{D}}}{I_{\text{D}} + I_{\text{R/N}}} \quad (2)$$

Other more details can be seen from the our previous work [2]. All potentials were converted to RHE.

### 2.3. Density functional theory (DFT) calculations

Dmol3 program of Materials studio is used to perform DFT calculations. The vacuum space was set at 20 Å. Other more details can be seen in Supporting information.

The adsorption energy ( $E_{\text{ads}}$ ) of ORR intermediates is calculated as follows:

$$E_{\text{ads}} = E_{\text{total}} - E_{\text{O}} - E_{\text{sub}} \quad (3)$$

Where  $E_{\text{total}}$  is total adsorption energy of catalyst and species,  $E_{\text{sub}}$  is the catalyst energy without adsorption,  $E_{\text{O}}$  is energy of species, Free energy change of every elementary reaction is calculated as follows:

$$\Delta G = \Delta E + T\Delta S + \Delta \text{ZPE} + \Delta G_{\text{field}} + \Delta G_{\text{U}} + \Delta G_{\text{pH}} \quad (4)$$

### 2.4. Assembly and tests of aqueous and all-solid-state Zn-air batteries

The aqueous Zn-air batteries (A-ZAB) were assembled with a nickel foam coated with the catalyst ink as an air cathode. Other more details can be found from the our previous work [2]. In brief, 2.5 mg of catalyst, 1 mg of acetylene black, and 4 mg of activated carbon were added to the solution, containing 8 μL of Nafion and 200 μL of isopropanol. The catalyst was applied dropwise to the surface of the nickel foam.

The assembled all-solid-state Zn-air battery (ASS-ZAB) was the same as that of ours previous work [20]. The performance of A-ZAB and ASS-ZAB were measured using CHI760E workstation and LAND CT2001A.

## 3. Results and discussion

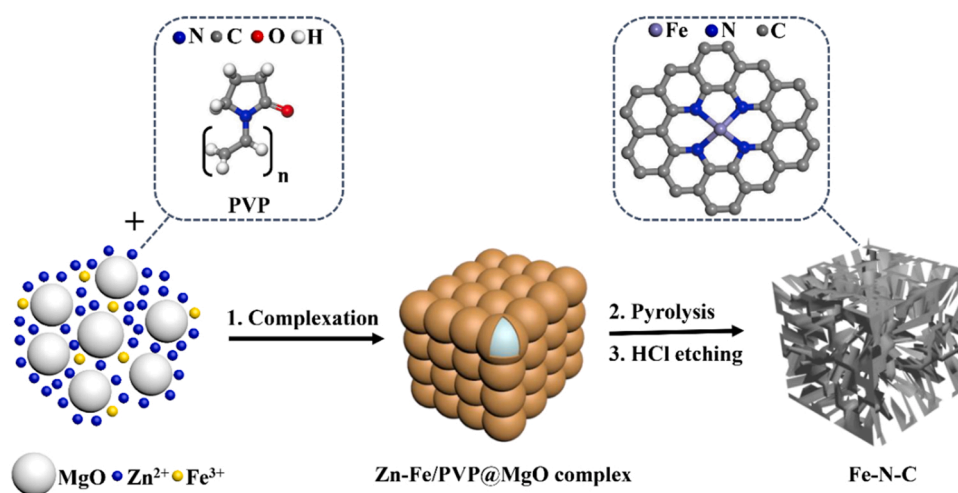
### 3.1. Synthesis and characterization of the Fe-N-C catalyst

As depicted in Scheme 1, Fe-N-C was prepared by a zinc-assisted MgO template strategy. First, Zn-Fe/PVP@MgO solid composites were prepared by freeze drying solution containing PVP, Zn(NO<sub>3</sub>)<sub>2</sub>·6 H<sub>2</sub>O, MgO and Fe(NO<sub>3</sub>)<sub>3</sub>·9 H<sub>2</sub>O. Here, the introduction of Zn nodes can isolate Fe cations and promote the production of abundant Fe-N<sub>x</sub> sites [22]. Then, the obtained sample was heated at 900 °C, which the Zn was easily vaporized, forming the rich micropores in the carbon substrate [20]. The carbonized material was treated with dilute hydrochloric acid for removing MgO template to obtain porous Fe-N-C. Besides, Fe-N-C/Zn was synthesized but without MgO under identical conditions. Similarly, Fe-N-C/Mg was synthesized without Zn(NO<sub>3</sub>)<sub>2</sub>·6 H<sub>2</sub>O. Fe-N-C/No was synthesized without Zn(NO<sub>3</sub>)<sub>2</sub>·6 H<sub>2</sub>O and MgO. N-C was synthesized without Fe(NO<sub>3</sub>)<sub>3</sub>·9 H<sub>2</sub>O.

The morphological characterizations reveal that zinc-assisted MgO template plays an important role in producing a porous structure. SEM image shows that Fe-N-C/No presents block-like morphology without porous structure under the absence of zinc-assisted MgO template (Fig. 1a), whereas Fe-N-C/Zn, Fe-N-C/Mg, and Fe-N-C possess porous structure (Fig. 1b-c and Fig. S2). TEM image (Fig. 1d) further confirms a porous feature in Fe-N-C. Obviously, diffraction ring could be only assigned to the graphitic carbon in selected-area diffraction patterns (SAED). Moreover, as shown in Fig. 1f, aberration-corrected (AC) HAADF-STEM demonstrates the presence of densely distributed single Fe atoms in Fe-N-C (Fe single atoms are marked by red circles). Elemental mapping images (Fig. 1g and Fig. S3c-f) and EELS (Fig. 2a) demonstrate the C, N and Fe elements coexist in Fe-N-C.

XRD patterns of Fe-N-C/Zn, Fe-N-C/Mg, and Fe-N-C show that three catalysts only possess two peaks (Fig. 2b), corresponding to characteristic planes of graphite [27,34,35]. In contrast, Fe-N-C/No exhibits that a set of sharp peaks can be assigned to the crystalline phase of Fe<sub>3</sub>C (JCPDS No. 35–0772), indicating that the zinc-assisted MgO template can effectively prevent the production of Fe<sub>3</sub>C. Moreover, Fe-N-C/No, Fe-N-C/Zn, Fe-N-C/Mg and Fe-N-C display a similar relatively low ratio of  $I_{\text{D}}/I_{\text{G}}$  as extracted from Raman spectrum (Fig. 2c), while the ratio of  $I_{\text{D}}/I_{\text{G}}$  of N-C (1.01) is much higher (Fig. S4), indicating that the template has no clear influence on the graphitic degree and the Fe can improve the graphitic degree of catalyst.

The N<sub>2</sub> physisorption experiments of catalysts are measured in Fig. 2d. Surface area (SA) in Fe-N-C is calculated to be 1061.45 m<sup>2</sup> g<sup>-1</sup>, higher than that of Fe-N-C/Zn (670.43 m<sup>2</sup> g<sup>-1</sup>), Fe-N-C/Mg (831.67 m<sup>2</sup> g<sup>-1</sup>), and Fe-N-C/No (105.05 m<sup>2</sup> g<sup>-1</sup>). Therefore, zinc-assisted MgO template could effectively increase the SA of catalysts. Pore size distribution (PSD) exhibit that Fe-N-C and Fe-N-C/Mg possess the micropores, mesopores, and macropores in Fig. 2e and f. Moreover, as depicted in the TEM image (Fig. S5), Fe-N-C exhibits the presence of the mesoporous and macropores (marked with red cycles, about 20–500 nm) in the carbon sheets. In contrast, PSD of Fe-N-C/Zn only shows the micropores (< 2 nm) and mesopores (about 4 nm) and no more additional



Scheme 1. A schematic synthesis process of the Fe-N-C catalyst.

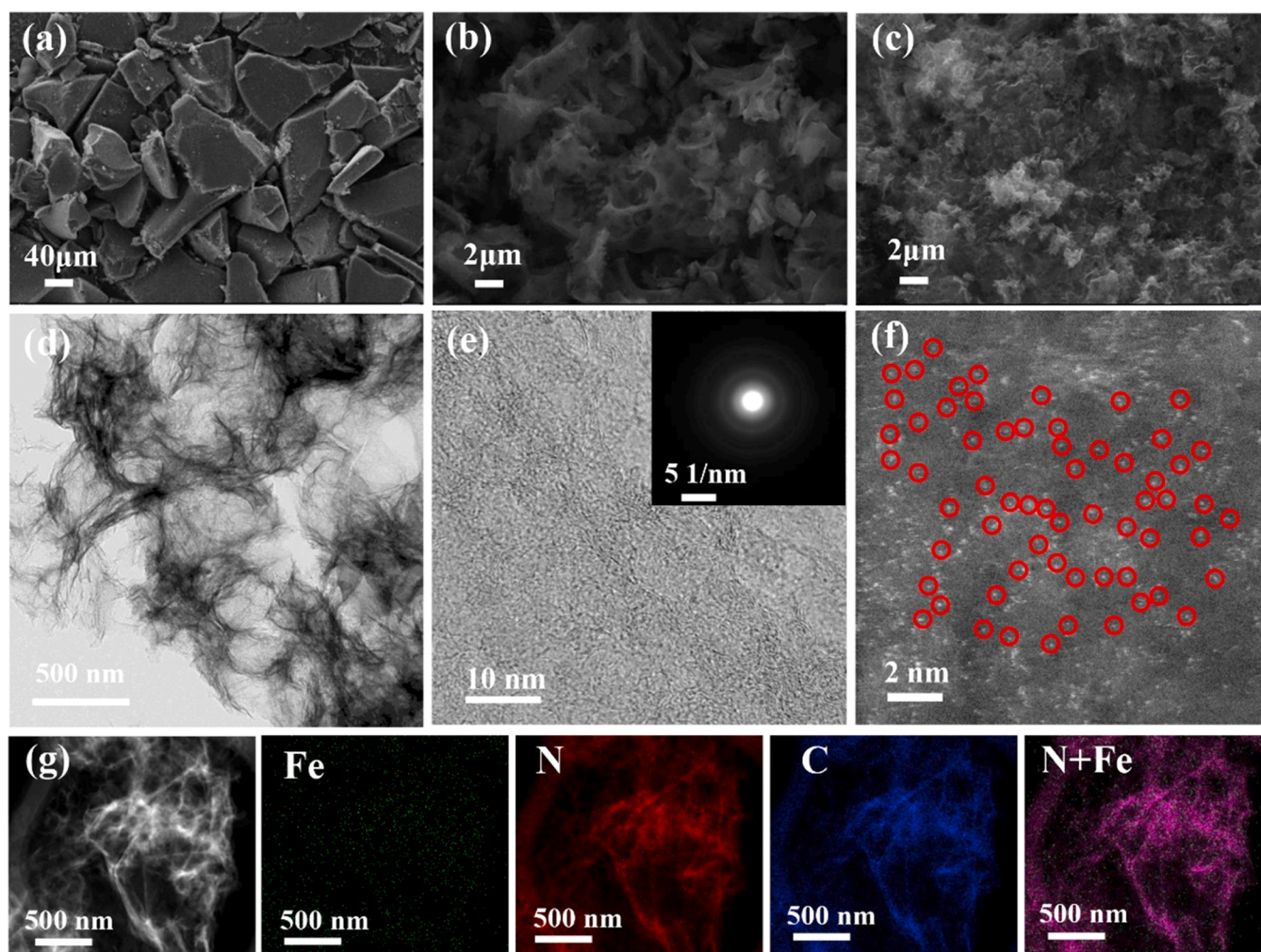


**Fig. 1.** (a-c) SEM images of Fe-N-C/No, Fe-N-C/Zn, and Fe-N-C. (d) TEM images of Fe-N-C. (e) and (f) High-resolution TEM images (inset: SAED) and AC HAADF-STEM of Fe-N-C. (g) The corresponding element mapping of Fe-N-C.

mesopores. However, for Fe-N-C/No, there is almost no pore structure in it. Therefore, the production of micropores and mesopores (about 4 nm) is attributed to evaporation of Zn, while the generation of mesopores and macropores by the removing of MgO template. Such the high SA and

hierarchical porous structure of Fe-N-C could effectively maximize the number of exposed Fe-N<sub>4</sub> sites and shorten the O<sub>2</sub> diffusion path, thereby significantly improving ORR activity [36].

XPS analysis is performed to prove the effect of zinc-assisted MgO



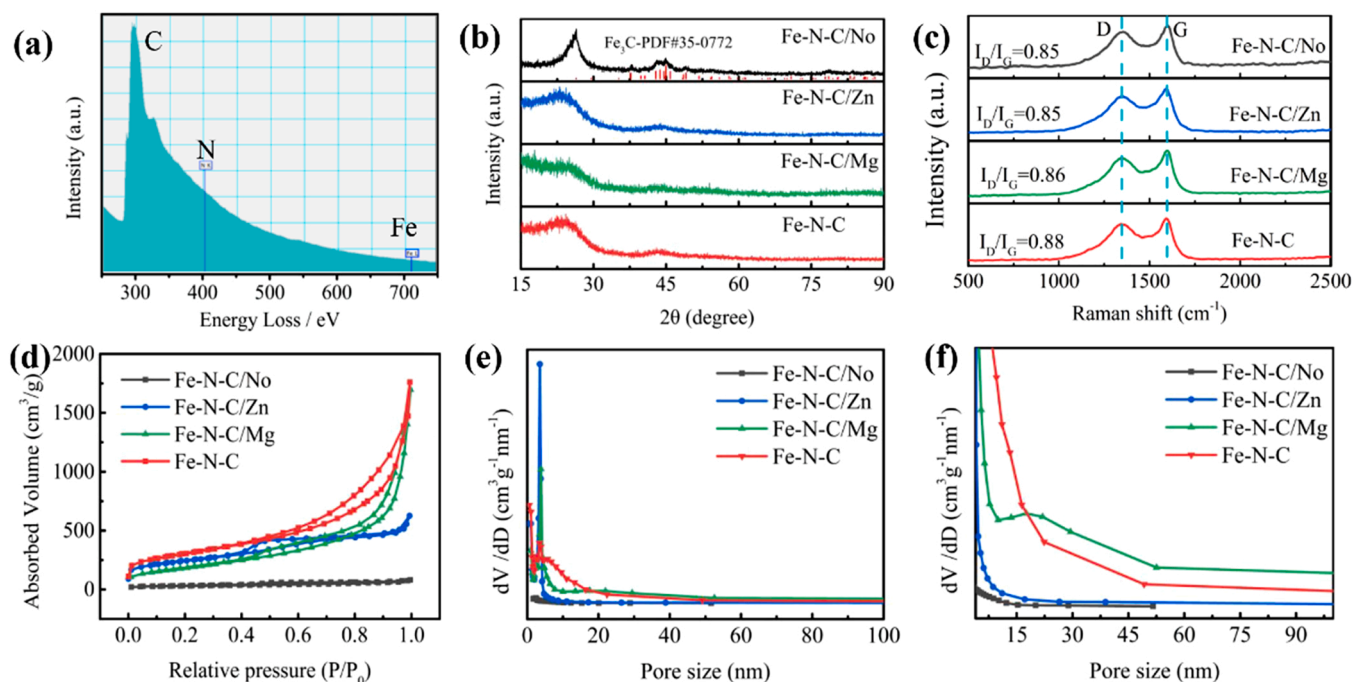


Fig. 2. (a) Electron energy loss spectroscopy (EELS) containing several dots of Fe-N-C. (b-f) XRD pattern, Raman spectra, N<sub>2</sub> adsorption-desorption isotherms, pore size distribution curves, and a magnified view (from 10 to 100 nm) for pore size distribution of Fe-N-C/Zn, Fe-N-C/Mg, and Fe-N-C.

template on surface composition in the catalysts. The peak signal of iron element cannot be detected (Fig. 3a-b), although EELS and elemental mapping analysis confirmed its presence. The absence of XPS signal of iron probably related to atomically dispersed iron form in Fe-N-C. The content of N and Fe in Fe-N-C are 3.18 and 0.32 at%, more than those of Fe-N-C/Zn (2.3 and 0.02 at%) and Fe-N-C/Mg (1.92 and 0.21 at%) in Fig. 3c and Table S1. However, the content of Fe (0.33 at%) in Fe-N-C/No is somewhat more than that of Fe-N-C, owing to the production of Fe<sub>3</sub>C. In addition, the content of Fe in Fe-N-C is 1.89 wt% by ICP-OES analysis, indicating that the zinc-assisted MgO template is beneficial for preventing the loss of nitrogen and forming Fe-N<sub>x</sub> sites. The high-resolution C1s spectrum (Fig. 3d) shows the prominent C-C (284.6), C-N (285.7) and C=O (289.1). The high-resolution N1s of catalysts can be deconvoluted into pyridinic N (398.6 ± 0.2 eV), pyrrolic N (400 ± 0.2 eV), graphitic N (401.2 ± 0.2 eV) and oxidized N (402.5 ± 0.2 eV) in Fig. 3e, respectively. The content of pyridinic N and graphitic N is highest for Fe-N-C among all catalysts (Fig. 3f), and is expected to promote ORR performance [37,38].

The coordination environment of Fe is confirmed by XAS. The Fe K-edge XANES exhibits that the curves of Fe-N-C close to that of the unheated iron phthalocyanine (FePc) in Fig. 3g. The EXAFS in Fig. 3h of Fe-N-C exhibits a peak located at about 1.5 Å, which is described as Fe-N coordination [39,40]. Meanwhile, the absence of peak at about 2.2 Å in Fe-N-C, which can be assigned to Fe-Fe coordination, implying that atomically dispersed Fe-N sites in Fe-N-C [8,17,41]. Furthermore, EXAFS fitting (Fig. S6 and Table S2) for the number of Fe configuration in Fe-N-C shows that each Fe atom can coordinate with four nitrogen atoms [42,43]. The above results indicate that porous carbon supported atomically dispersed Fe-N<sub>4</sub> sites have been successfully synthesized [44], and corresponding structural features of Fe-N<sub>4</sub> active sites in Fig. 3i.

### 3.2. Electrochemical evaluation of ORR activity

CV curves are firstly tested to preliminarily evaluate ORR activity in Fig. S7. Fe-N-C shows the most positive ORR peak potential among all catalysts, indicating that Fe-N-C has the highest ORR activity [45].

Linear sweep voltammetry is measured to evaluate activity (Fig. 4a). Fe-N-C delivers the highest activity with a  $E_{1/2}$  of 0.895 V, surpassing that of Pt/C (0.845 V), Fe-N-C/Zn (0.872 V), and Fe-N-C/Mg (0.851 V), revealing that zinc-assisted MgO template can efficiently enhance ORR activity. Such an advanced activity, which comparable to most advanced Pt-free catalysts (Table S3)[46,47]. Furthermore, ORR activity is also measured in 0.1 M HClO<sub>4</sub>, which conveys a  $E_{1/2}$  of 0.761 V in Fe-N-C (Fig. S8). Meanwhile, the durability of Fe-N-C show a  $E_{1/2}$  loss of only 14 mV after 5000 cycles (Fig. S9).

The kinetic current density ( $j_k$ ) of Fe-N-C is up to 37.81 mA cm<sup>-2</sup>, which is 7.52-fold that of Pt/C (5.03 mA cm<sup>-2</sup>) in Fig. 4b. Furthermore, Fe-N-C displays the lowest Tafel slope (54.62 mV dec<sup>-1</sup>) among all catalysts in Fig. 4c, reflecting a fast electrochemical kinetic toward ORR. The reaction kinetics is additionally evaluated by electrochemical impedance spectra (EIS) in Fig. 4d. Fe-N-C exhibits the lowest charge transfer resistance ( $R_{ct}$ ), suggesting that zinc-assisted MgO template strategy can reduce  $R_{ct}$  and accelerate electron transfer, thus promoting the ORR kinetics. RRDE are measured to quantify the ORR pathway. The yield of H<sub>2</sub>O<sub>2</sub> in Fe-N-C maintains less than 3%, and electron transfer number of Fe-N-C is 3.94–3.99 in the range from 0.6 to 1.0 V (Fig. 4e), demonstrating a superior selectivity toward H<sub>2</sub>O and a 4-electron during ORR process.

The double-layer capacitance ( $C_{dl}$ ) of Fe-N-C (47.18 mF cm<sup>-2</sup>) is higher than those of Fe-N-C/Zn (22.82 mF cm<sup>-2</sup>) and Fe-N-C/Mg (40.25 mF cm<sup>-2</sup>), indicating that zinc-cooperated MgO template can increase the accessibility to active sites (Fig. 4f and Figs. S10). Accelerated durability test (ADT) is measured to evaluate the durability of Fe-N-C. As depicted in Figs. 4g and 4h, the  $E_{1/2}$  of Fe-N-C exhibits a minor loss of 7 mV after ADT, less than that of Pt/C (15 mV), suggesting superior ORR stability. The methanol tolerance of catalysts is evaluated in Fig. 4i. Remarkably, the current of Fe-N-C only fluctuates slightly when methanol is injected, while that of Pt/C exhibits drastic fluctuation, revealing a better tolerance to methanol of Fe-N-C than Pt/C.

ORR performance of Fe-N-C is related to the density of Fe-N<sub>4</sub> sites. Therefore, site density (SD) and utilization rate of Fe-N<sub>4</sub> sites by a previously reported nitrite reduction method [48] in Fig. S11a and b. The SD of Fe-N-C is  $6.237 \times 10^{19}$  site g<sup>-1</sup> and the utilization of Fe-N<sub>4</sub> sites is



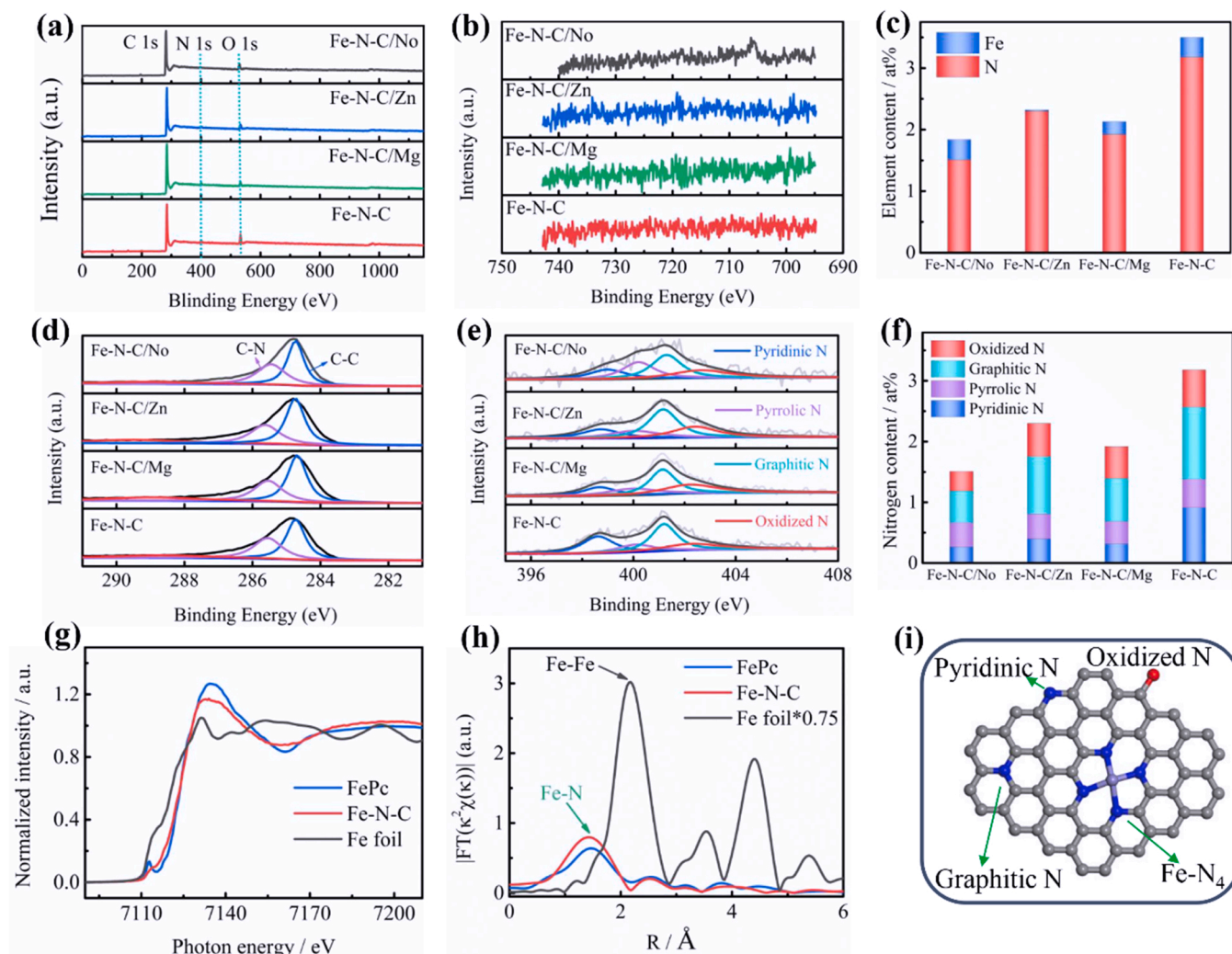
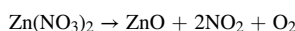


**Fig. 3.** (a) XPS survey spectrum. (b) Fe 2p region. (c) Fe and N content by XPS survey (d) C1s region. (e) N1s region, and (f) Proportion statistics for each N species of Fe-N-C/Zn, Fe-N-C/Mg, and Fe-N-C. (g) Fe K-edge XANES and (h) Fourier transforms of EXAFS spectra of Fe-N-C and references. (i) Structural features of pyridinic-N, graphitic-N, and Fe-N.

40.11%. Fig. S11c shows the steps of nitrite adsorption and subsequent reductive stripping.

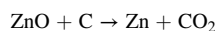
### 3.3. The formation mechanism of dense atomic Fe-N<sub>4</sub> active sites

According to the above experimental and analytical results, zinc-assisted MgO template is a satisfactory method to improve ORR performance. To reveal the nature of the enhanced ORR performance, XRD patterns are carried out to characterize Zn-Fe/PVP@MgO solid composites calcined at 200, 400, 600, 800 and 900 °C (without any post-processing). As shown in Fig. S12a, Zn ion are converted into ZnO (JCPDS No. 36–1451) at 200 °C. Other diffraction peaks can be ascribed to the MgO template (JCPDS No. 45–0946). Therefore, as the temperature goes up, Zn(NO<sub>3</sub>)<sub>2</sub> could be converted to ZnO [49], and the corresponding reaction is shown as follows:



When the temperature is between 200 °C and 800 °C, the ZnO is relatively stable, which is detected from the result of XRD patterns (Fig. S12a, b, c, and d). During this period, only XRD peaks for ZnO and MgO can be observed. In this case, these ZnO species can isolate and surround Fe atoms [22], preventing Fe atoms from aggregating into Fe<sub>3</sub>C, which is beneficial to achieve dense Fe-N<sub>4</sub> active sites. As the

temperature increases, ZnO species are converted into metallic Zn by carbothermal reduction, and the chemical reaction is shown as follows [50]:



Finally, as seen from Fig. S12e, the diffraction peaks for ZnO are disappeared at 900 °C, which is attributed to the evaporation of Zn, thus creating porous structure in the carbon framework at 900 °C [23]. Meanwhile, MgO template can produce mesopores and macropores in carbon matrix by etching treatment with a mild HCl solution.

Based on the above results, the formation mechanism of the Fe-N-C is analyzed in Fig. 5a. With the help of zinc-assisted MgO template, dense Fe-N<sub>4</sub> sites of Fe-N-C is obtained and the Fe content in that is the highest (Fig. 3c). By contrast, for Fe-N-C/Mg, most Fe atoms are converted into Fe containing nanoparticles without the constraints of Zn node in Fig. 5b. Consequently, the content of Fe-N<sub>4</sub> sites in Fe-N-C/Mg is relatively less than that of Fe-N-C.

In addition, the MgO template remains stable in particle size and structure during pyrolysis, while the structure of Zn species changes with temperature and eventually evaporates at 900 °C. Therefore, MgO template with stable structure may be more conducive to expanding the distance of adjacent Fe ions, resulting in higher Fe content in the sample. Therefore, for synthesis of Fe-N-C/Zn, the content of Fe in Fe-N-C/Zn is

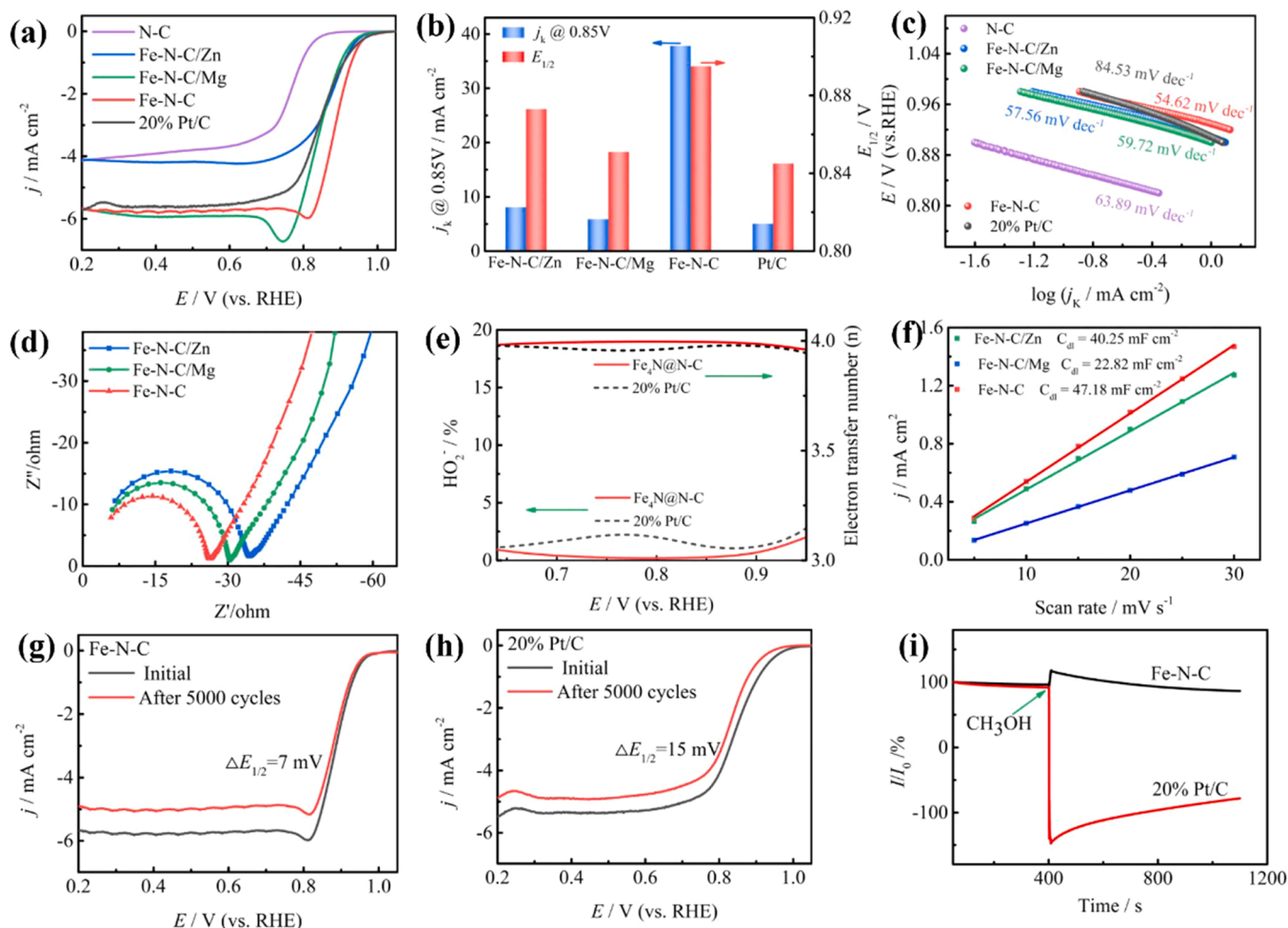


**Fig. 4.** (a) ORR polarization curves in 0.1 M KOH with a rotating speed of 1600 rpm at the scan rate of 10 mV s<sup>-1</sup>. (b)  $j_k$  at 0.85 V and  $E_{1/2}$  of catalysts. (c) Tafel plots of catalysts. (d) Electrochemical impedance spectroscopy of catalysts. (e)  $\text{HO}_2^-$  yield and electron transfer number plots of Fe-N-C and Pt/C. (f) Electrochemical double-layer capacitance ( $C_{dl}$ ) of catalysts. (g) and (h) ORR polarization curves before and after 5000 CV cycles of Fe-N-C and Pt/C in 0.1 M KOH. (i) I-t CA responses for Fe-N-C and Pt/C at 0.75 V with 1600 rpm when 8 mL of methanol addition in 50 mL of electrolyte at around 400 s.

the lowest without MgO template. These analytical results imply that zinc-cooperated MgO template can effectively increase porous structure to host atomic accessibly abundant Fe-N<sub>4</sub> sites and thus boost ORR activity.

### 3.4. Theoretical evaluation on ORR activity

To elucidate the nature of Fe-N<sub>4</sub> sites supported on Fe-N-C for efficient ORR activity, DFT calculations are performed to gain further insights on ORR mechanism. The computational model of Pt (111) and Fe-N<sub>4</sub> are presented in Fig. S13. Fig. 6a and Fig. S14 display that the optimal structures of ORR intermediates which are adsorbed on Fe-N<sub>4</sub> site and Pt (111), respectively. As shown in Table S4, all the negative adsorption energies ( $E_{ads}$ ) indicate that ORR intermediates can be stably adsorbed on Fe-N<sub>4</sub> site and Pt (111), which are efficient to initiate the ORR. The 4-electron ORR mechanism for Fe-N<sub>4</sub> site is shown in Fig. 6b. Figs. 6c and 6d show the free-energy of ORR reaction process of Fe-N<sub>4</sub> site and Pt (111), respectively. Interestingly, the Fe-N<sub>4</sub> site exhibits a lower limiting energy barrier of 1.04 eV (the rate-determining step is from OH\* to OH) than that (1.13 eV) of Pt (111) (the rate-determining step is from O<sub>2</sub> to OOH\*). Furthermore, the limiting potential of Fe-N<sub>4</sub> site (0.19 V) is higher than that of Pt (111) (0.10 V), indicating a superior ORR performance of Fe-N<sub>4</sub> site [51]. Therefore, Fe-N-C possesses excellent ORR performance due to dense Fe-N<sub>4</sub> active center, which is well consistent with our experimental result.

### 3.5. Electrochemical performance of aqueous Zn-air batteries

Due to outstanding ORR activity for Fe-N-C, the aqueous Zn-air battery (A-ZAB) is assembled to explore the practical application (Fig. 7a). Fig. 7b presents an open-circuit voltage (OCV) of 1.479 V for Fe-N-C based A-ZAB (Fe-N-C A-ZAB). The continuous OCV is also examined in Fig. 7c. Notably, the OCV of Fe-N-C A-ZAB is up to 1.47 V. As demonstrated in Fig. 7d, Fe-N-C A-ZAB shows a power density of 175 mW cm<sup>-2</sup>, superior to that of Pt/C A-ZAB (102 mW cm<sup>-2</sup>) and most of the reported Pt-free catalysts (Table S5).

The galvanostatic discharge tests are carried out at various current densities in Fig. 7e, where Fe-N-C A-ZAB displays the superior rate performance. Furthermore, no significant potential change in Fe-N-C A-ZAB can be detected for 100 h (Fig. 7f), indicating great potential of Fe-N-C in a stable practical application performance. Meanwhile, Fe-N-C A-ZAB delivers a specific capacity of 775.7 mAh g<sub>Zn</sub><sup>-1</sup> (Fig. 7g), higher than that of Pt/C A-ZAB (714.3 mAh g<sub>Zn</sub><sup>-1</sup>). In addition, Fig. S15 presents Fe-N-C A-ZAB has a energy density of 1040 Wh kg<sup>-1</sup>, which outperforms the Pt/C A-ZAB (912 Wh kg<sup>-1</sup>).

Fe-N-C A-ZABs could easily power up a series of LED and electric fan in Fig. 7h. As an ORR catalyst, Fig. 7i illustrates the porous structure advantages in Fe-N-C. Moreover, Fe-N-C A-ZAB shows that no obvious increase in the charge/discharge voltage gap even after about 643 h (3860 cycles) cycling test in Fig. 7j, demonstrating an excellent long-term cycling performance. The porous structure ensures Fe-N<sub>4</sub> sites

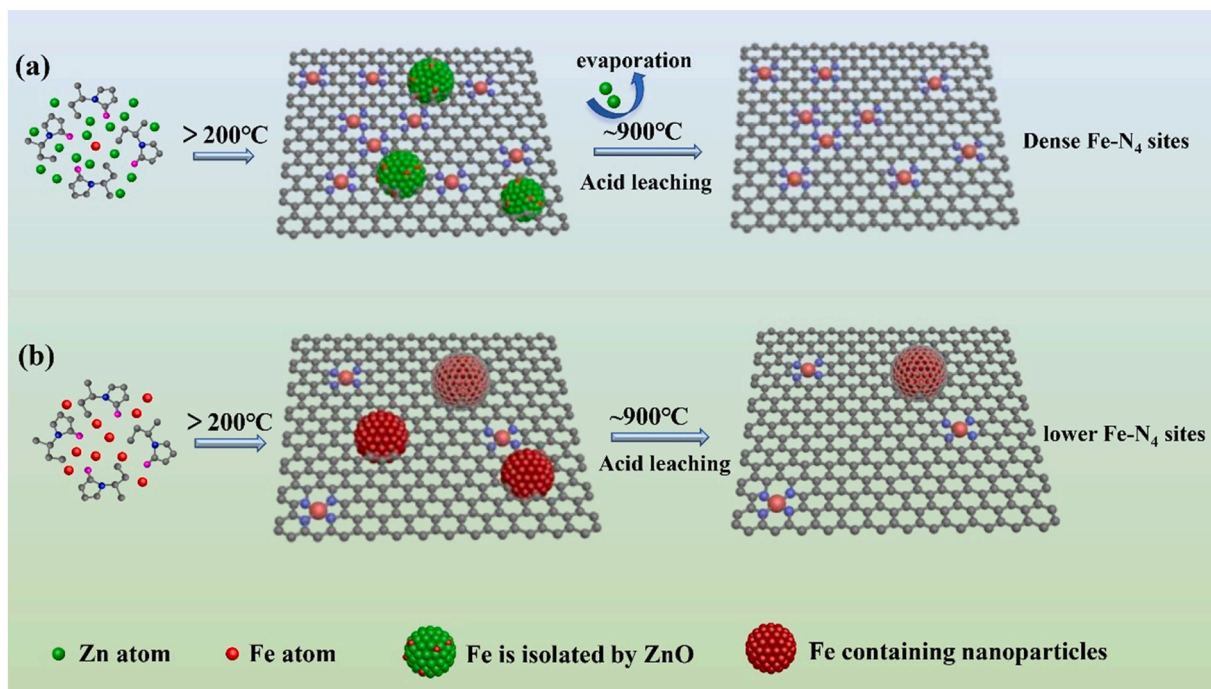
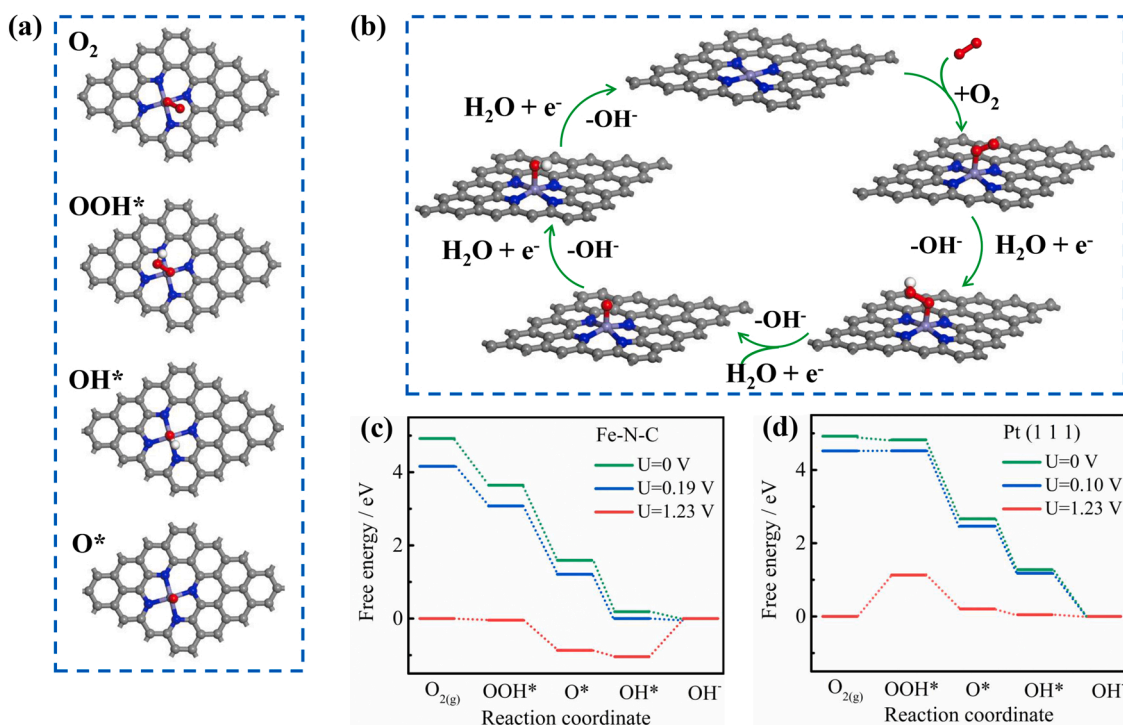


Fig. 5. Schematic formation mechanism of (a) Fe-N-C, (b) Fe-N-C/No.

Fig. 6. (a) The adsorption configurations of ORR intermediates on the Fe-N<sub>4</sub> site. (b) The proposed ORR mechanism on Fe-N<sub>4</sub> site under alkaline condition. (c) and (d) Free energy diagrams for ORR of Fe-N<sub>4</sub> and Pt (111).

are fully exposed and effectively improves the accessibility of active sites during ORR.

### 3.6. Electrochemical performance of all-solid-state Zn-air batteries

ASS-ZAB is assembled as illustrated in Fig. 8a. The PVA film is employed as a solid electrolyte in Fig. 8b. The OCV of Fe-N-C ASS-ZAB is measured by a voltmeter and a value of 1.496 V obtained (Fig. 8c). The

OCV of Fe-N-C ASS-ZAB is also measured 1.52 V in Fig. 8d. Notably, Fe-N-C ASS-ZAB displays a peak power density of  $112\text{ mW cm}^{-2}$  (Fig. 8e), better than that of Pt/C ASS-ZAB ( $94\text{ mW cm}^{-2}$ ) and most of the Pt-free catalysts (Table S5). Fe-N-C ASS-ZAB exhibits a long lifetime for discharging about 14 h (Fig. 8f). When charge-discharge cycling test is carried out (Fig. 8g), the voltage of the Fe-N-C ASS-ZAB keeps stable, while Pt/C ASS-ZAB shows severe voltage decrease, especially in discharge process. An excellent cyclability of Fe-N-C ASS-ZAB can be



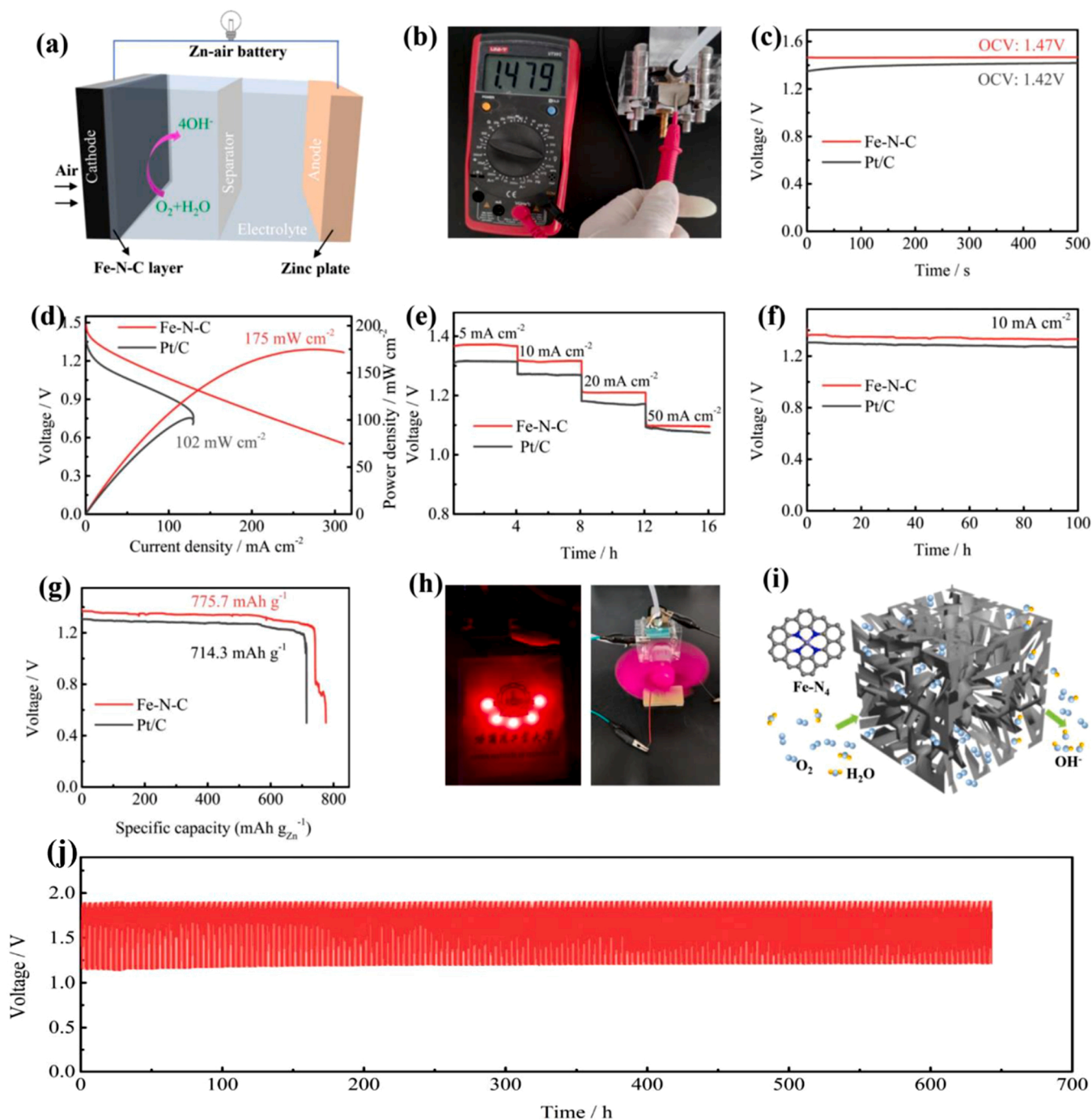


**Fig. 7.** (a) Schematic illustration of an as-assembled A-ZAB. (b) Photograph of the Fe-N-C A-ZAB with an open-circuit voltage of 1.479 V. (c) Open-circuit plots of Fe-N-C and Pt/C. (d) Polarization and power density curves for primary Zn-air batteries. (e) Discharge curves of the A-ZAB assembled with Fe-N-C at current densities of 5, 10, 20, 50 mA cm<sup>-2</sup> for 4 h. (f) Discharge curves of A-ZAB at 10 mA cm<sup>-2</sup> for 100 h. (g) Specific capacities plots at 10 mA cm<sup>-2</sup>. (h) Photograph of red LED and fan are driven by Fe-N-C based Zn-air batteries. (i) Schematic illustration of Fe-N-C for efficient ORR electrocatalysis. (j) Cycling performance of the Fe-N-C A-ZAB at a current density of 5 mA cm<sup>-2</sup> (6 M KOH with 0.2 M zinc acetate was used as the electrolyte).

observed at long charge-discharge periods (5.5 h), indicating the great application potential in rechargeable ASS-ZAB. A Fe-N-C ASS-ZAB could effectively power a fan (Fig. 8h) and two connected Fe-N-C ASS-ZAB could power a yellow LED (Fig. 8i), revealing the promising potential of Fe-N-C in flexible devices.

### 3.7. The insight into O<sub>2</sub> diffusion mechanism

In order to further insight into the O<sub>2</sub> diffusion in the prepared catalyst air cathode, COMSOL Multiphysics finite-element-based solver

is employed to unveil the O<sub>2</sub> diffusion mechanism in the catalyst layer [30]. As shown in Fig. 9a, O<sub>2</sub> diffusion is simulated in the catalyst, and the contour plot of O<sub>2</sub> concentration is obtained. Clearly, Fe-N-C shows a higher O<sub>2</sub> concentration in the internal of catalyst layer, whereas Fe-N-C/No shows a lower O<sub>2</sub> concentration (Fig. 9b). The Fe-N-C catalyst layer exhibits a thin porous framework, which ensures the significantly exposed of Fe-N<sub>4</sub> sites and could accelerate the diffusion of O<sub>2</sub>, resulting in sufficient catalysts/electrolyte/O<sub>2</sub> three-phase boundary for ORR and thus improve cell performance. Whereas, the Fe-N-C/No exhibits thick block-like layer without porous structure, which would limit

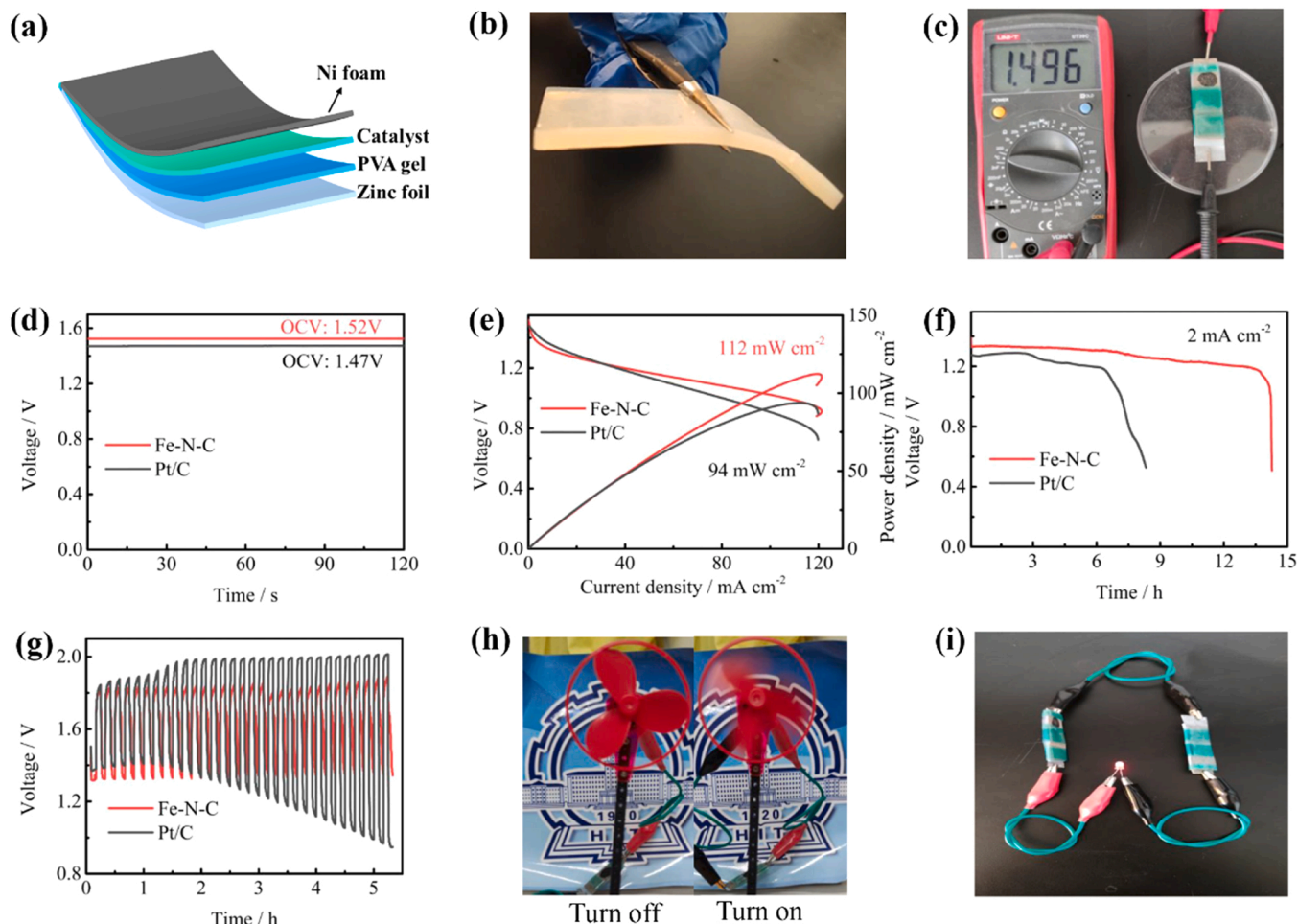


**Fig. 8.** (a) Schematic illustration of ASS-ZAB configuration. (b) Photograph of the solid-state electrolyte. (c) Photograph of the Fe-N-C ASS-ZAB with an open-circuit voltage. (d) Open-circuit plots for ASS-ZABs. (e) Polarization and power density curves for ASS-ZABs. (f) Discharge curves of ASS-ZABs at  $2 \text{ mA cm}^{-2}$ . (g) Charge and discharge curves of ASS-ZAB at  $5 \text{ mA cm}^{-2}$ . (h) Photograph of fan is powered by one Fe-N-C ASS-ZAB. (i) Photograph of LED is lighted up by two Fe-N-C ASS-ZABs.

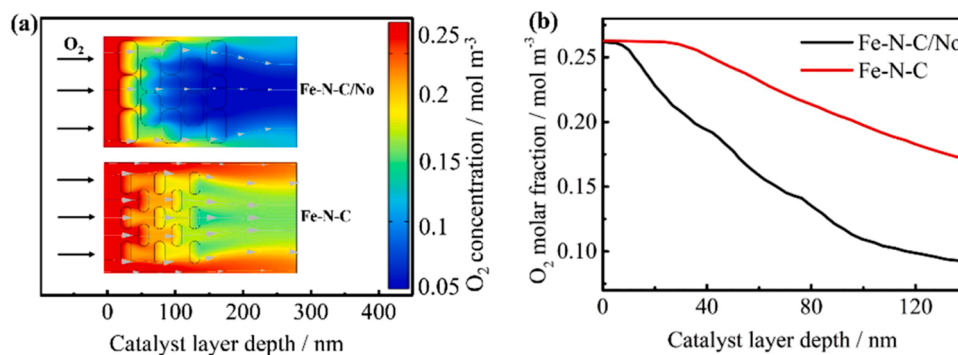


**Fig. 9.** (a) COMSOL Multiphysics Model of  $\text{O}_2$  diffusion into Fe-N-C and Fe-N-C/No air electrode. (b) The  $\text{O}_2$  molar fraction distribution of Fe-N-C and Fe-N-C/No air electrode.

the  $\text{O}_2$  diffusion, thereby leading to unsatisfactory cell performance.

#### 4. Conclusions

In conclusion, a facile zinc-assisted template strategy was developed for the successful preparation of porous Fe-N-C. Owing to its accessibly abundant  $\text{Fe-N}_4$  sites, the Fe-N-C exhibits outstanding  $E_{1/2}$  of 0.895 V and excellent durability of only 7 mV decreases after ADT in alkaline medium, surpassing the Pt/C. The theoretical calculations manifest that

the high ORR activity is attributed to  $\text{Fe-N}_4$  active sites, which significantly reduces the energy barriers in ORR process. Meanwhile, finite element simulation exhibits that a porous framework of Fe-N-C could significantly accelerate the diffusion of  $\text{O}_2$  and thus improve cell performance. Therefore, Fe-N-C based Zn-air batteries possess excellent discharge ability and durability. The suggested novel synthesis procedures would be helpful for the further development of atomically dispersed Metal-N-C catalysts for ORR.

## CRediT authorship contribution statement

**Xiangyu Lu:** Conceptualization, Data curation, Writing – original draft. **Hao Xu:** Formal Analysis, Investigation. **Peixia Yang:** Conceptualization, Funding acquisition, Project administration, Writing – review & editing. **Lihui Xiao:** Investigation, Software. **Yaqiang Li:** Investigation, Software. **Jingyuan Ma:** Software, Writing – review & editing, Resources. **Ruopeng Li:** Investigation. **Lilai Liu:** Funding acquisition, Resources. **Anmin Liu:** Software. **Veniamin Kondratiev:** Writing – review & editing. **Oleg Levin:** Writing – review & editing. **Jinqiu Zhang:** Funding acquisition, Resources. **Maozhong An:** Funding acquisition, Resources.

## Declaration of Competing Interest

The authors declare that they have no known competing financial interests or personal relationships that could have appeared to influence the work reported in this paper.

## Acknowledgements

This work was supported by NSFC-RFBR Joint Research Project (No. 22111530014 (NSFC) and 21-53-53034 (RFBR)), Natural Science Foundation of Heilongjiang Province (No. LH2021B026) and National Natural Science Foundation of China (No.21878061). The authors would like to thank Shiyanjia Lab ([www.shiyanjia.com](http://www.shiyanjia.com)) for the XPS. The numerical calculations in this paper have been done on Harbin advanced computing center.

## Appendix A. Supporting information

Supplementary data associated with this article can be found in the online version at [doi:10.1016/j.apcatb.2022.121454](https://doi.org/10.1016/j.apcatb.2022.121454).

## References

- J. Han, H. Bao, J.-Q. Wang, L. Zheng, S. Sun, Z.L. Wang, C. Sun, 3D N-doped ordered mesoporous carbon supported single-atom Fe-N-C catalysts with superior performance for oxygen reduction reaction and zinc-air battery, *Appl. Catal. B Environ.* 280 (2021), 119411, <https://doi.org/10.1016/j.apcatb.2020.119411>.
- D. Wang, H. Xu, P. Yang, X. Lu, J. Ma, R. Li, L. Xiao, J. Zhang, M. An, Fe-N<sub>4</sub> and Co-N<sub>4</sub> dual sites for boosting oxygen electroreduction in Zn-air batteries, *J. Mater. Chem. A* 9 (2021) 13678–13687, <https://doi.org/10.1039/d1ta03176g>.
- Y.-N. Sun, J. Yang, X. Ding, W. Ji, A. Jaworski, N. Hedin, B.-H. Han, Synergetic contribution of nitrogen and fluorine species in porous carbons as metal-free and bifunctional oxygen electrocatalysts for zinc-air batteries, *Appl. Catal. B Environ.* 297 (2021), 120448, <https://doi.org/10.1016/j.apcatb.2021.120448>.
- D. Wang, P. Yang, H. Xu, J. Ma, L. Du, G. Zhang, R. Li, Z. Jiang, Y. Li, J. Zhang, M. An, The dual-nitrogen-source strategy to modulate a bifunctional hybrid Co/Co-N-C catalyst in the reversible air cathode for Zn-air batteries, *J. Power Sources* 485 (2021), 229339, <https://doi.org/10.1016/j.jpowsour.2020.229339>.
- N. Logeshwaran, S. Ramakrishnan, S.S. Chandrasekaran, M. Vinothkannan, A. R. Kim, S. Sengodan, D.B. Velusamy, P. Varadhan, J.-H. He, D.J. Yoo, An efficient and durable trifunctional electrocatalyst for zinc-air batteries driven overall water splitting, *Appl. Catal. B Environ.* 297 (2021), 120405, <https://doi.org/10.1016/j.apcatb.2021.120405>.
- J. Wang, J. Xu, X. Guo, T. Shen, C. Xuan, B. Tian, Z. Wen, Y. Zhu, D. Wang, Synergistic regulation of nickel doping/hierarchical structure in cobalt sulfide for high performance zinc-air battery, *Appl. Catal. B Environ.* 298 (2021), 120539, <https://doi.org/10.1016/j.apcatb.2021.120539>.
- N.R. Sahraie, U.I. Kramm, J. Steinberg, Y. Zhang, A. Thomas, T. Reier, J. P. Paraknowitsch, P. Strasser, Quantifying the density and utilization of active sites in non-precious metal oxygen electroreduction catalysts, *Nat. Commun.* 6 (2015) 8618, <https://doi.org/10.1038/ncomms9618>.
- J. Wang, Z. Huang, W. Liu, C. Chang, H. Tang, Z. Li, W. Chen, C. Jia, T. Yao, S. Wei, Y. Wu, Y. Li, Design of N-coordinated dual-metal sites: a stable and active Pt-free catalyst for acidic oxygen reduction reaction, *J. Am. Chem. Soc.* 139 (2017) 17281–17284, <https://doi.org/10.1021/jacs.7b10385>.
- X. Lu, L. Du, D. Wang, P. Yang, L. Liu, J. Zhang, M. An, O. Levin, J. Wang, L. Ge, Highly dispersed Cu-N<sub>x</sub> moieties embedded in graphene: a promising electrocatalyst towards the oxygen reduction reaction, *Chemelectrochem* 5 (2018) 3323–3329, <https://doi.org/10.1002/celec.201800657>.
- H. Xu, D. Wang, P. Yang, A. Liu, R. Li, L. Xiao, J. Zhang, Z. Qu, M. An, FeS encapsulated hierarchical porous S, N-dual-doped carbon for oxygen reduction reaction facilitation in Zn-air batteries, *Sustainable, Energy Fuels* 5 (2021) 2695–2703, <https://doi.org/10.1039/d1se00242b>.
- F. Liu, L. Shi, X. Lin, D. Yu, C. Zhang, R. Xu, D. Liu, J. Qiu, L. Dai, Site-density engineering of single-atomic iron catalysts for high-performance proton exchange membrane fuel cells, *Appl. Catal. B Environ.* 302 (2022), 120860, <https://doi.org/10.1016/j.apcatb.2021.120860>.
- D. Wang, L. Xiao, P. Yang, Z. Xu, X. Lu, L. Du, O. Levin, L. Ge, X. Pan, J. Zhang, M. An, Dual-nitrogen-source engineered Fe-N<sub>x</sub> moieties as a booster for oxygen electroreduction, *J. Mater. Chem. A* 7 (2019) 11007–11015, <https://doi.org/10.1039/c9ta01953g>.
- D. Wang, X. Pan, P. Yang, R. Li, H. Xu, Y. Li, F. Meng, J. Zhang, M. An, Transition metal and nitrogen Co-doped carbon-based electrocatalysts for the oxygen reduction reaction: from active site insights to the rational design of precursors and structures, *ChemSusChem* 14 (2021) 33–55, <https://doi.org/10.1002/cssc.202002137>.
- J. Tian, A. Morozan, M.T. Sougrati, M. Lefevre, R. Chenitz, J.P. Dodelet, D. Jones, F. Jaouen, Optimized synthesis of Fe/N/C cathode catalysts for PEM fuel cells: a matter of iron-ligand coordination strength, *Angew. Chem. Int. Ed. Engl.* 52 (2013) 6867–6870, <https://doi.org/10.1002/anie.201303025>.
- Y. Li, P. Zhang, L. Wan, Y. Zheng, X. Qu, H. Zhang, Y. Wang, K. Zaghib, J. Yuan, S. Sun, Y. Wang, Z. Zhou, S. Sun, A general carboxylate-assisted approach to boost the ORR performance of ZIF-derived Fe/N/C catalysts for proton exchange membrane fuel cells, *Adv. Funct. Mater.* 31 (2021) 2009645, <https://doi.org/10.1002/adfm.202009645>.
- Z. Yang, Y. Wang, M. Zhu, Z. Li, W. Chen, W. Wei, T. Yuan, Y. Qu, Q. Xu, C. Zhao, X. Wang, P. Li, Y. Li, Y. Wu, Y. Li, Boosting oxygen reduction catalysis with Fe-N<sub>4</sub> sites decorated porous carbons toward fuel cells, *ACS Catal.* 9 (2019) 2158–2163, <https://doi.org/10.1021/acscatal.8b04381>.
- H. Yang, Z. Li, S. Kou, G. Lu, Z. Liu, A complex-sequestered strategy to fabricate Fe single-atom catalyst for efficient oxygen reduction in a broad pH-range, *Appl. Catal. B Environ.* 278 (2020), 119270, <https://doi.org/10.1016/j.apcatb.2020.119270>.
- H. Xu, D. Wang, P. Yang, A. Liu, R. Li, Y. Li, L. Xiao, X. Ren, J. Zhang, M. An, Atomically dispersed M-N-C catalysts for the oxygen reduction reaction, *J. Mater. Chem. A* 8 (2020) 23187–23201, <https://doi.org/10.1039/d0ta08732g>.
- H. Xu, D. Wang, P. Yang, A. Liu, R. Li, Y. Li, L. Xiao, J. Zhang, M. An, A theoretical study of atomically dispersed MN<sub>4</sub>/C (M = Fe or Mn) as a high-activity catalyst for the oxygen reduction reaction, *Phys. Chem. Chem. Phys.* 22 (2020) 28297–28303, <https://doi.org/10.1039/d0cp04676k>.
- D. Wang, H. Xu, P. Yang, L. Xiao, L. Du, X. Lu, R. Li, J. Zhang, M. An, A dual-template strategy to engineer hierarchically porous Fe-N-C electrocatalysts for the high-performance cathodes of Zn-air batteries, *J. Mater. Chem. A* 9 (2021) 9761–9770, <https://doi.org/10.1039/d1ta00585e>.
- J. Woo, S.Y. Yang, Y.J. Sa, W.-Y. Choi, M.-H. Lee, H.-W. Lee, T.J. Shin, T.-Y. Kim, S. H. Joo, Promoting oxygen reduction reaction activity of Fe-N/C electrocatalysts by silica-coating-mediated synthesis for anion-exchange membrane fuel cells, *Chem. Mater.* 30 (2018) 6684–6701, <https://doi.org/10.1021/acs.chemmater.8b02117>.
- J.-C. Li, F. Xiao, H. Zhong, T. Li, M. Xu, L. Ma, M. Cheng, D. Liu, S. Feng, Q. Shi, H.-M. Cheng, C. Liu, D. Du, S.P. Beckman, X. Pan, Y. Lin, M. An, Secondary-atom-assisted synthesis of single iron atoms anchored on N-doped carbon nanowires for oxygen reduction reaction, *ACS Catal.* 9 (2019) 5929–5934, <https://doi.org/10.1021/acscatal.9b00869>.
- G. Chen, P. Liu, Z. Liao, F. Sun, Y. He, H. Zhong, T. Zhang, E. Zschech, M. Chen, G. Wu, J. Zhang, X. Feng, Zinc-mediated template synthesis of Fe-N-C electrocatalysts with densely accessible Fe-N<sub>x</sub> active sites for efficient oxygen reduction, *Adv. Mater.* 32 (2020) 1907399, <https://doi.org/10.1002/adma.201907399>.
- X. Lu, L. Ge, P. Yang, O. Levin, V. Kondratiev, Z. Qu, L. Liu, J. Zhang, M. An, N-doped carbon nanosheets with ultra-high specific surface area for boosting oxygen reduction reaction in Zn-air batteries, *Appl. Surf. Sci.* 562 (2021), 150114, <https://doi.org/10.1016/j.apsusc.2021.150114>.
- L. Jiao, J. Li, L.L. Richard, Q. Sun, T. Stracensky, E. Liu, M.T. Sougrati, Z. Zhao, F. Yang, S. Zhong, H. Xu, S. Mukerjee, Y. Huang, D.A. Cullen, J.H. Park, M. Ferrandon, D.J. Myers, F. Jaouen, Q. Jia, Chemical vapour deposition of Fe-N-C oxygen reduction catalysts with full utilization of dense Fe-N<sub>4</sub> sites, *Nat. Mater.* 20 (2021) 1385–1391, <https://doi.org/10.1038/s41563-021-01030-2>.
- H. Adabi, A. Shakouri, N. Ul Hassan, J.R. Varcoe, B. Zulevi, A. Serov, J. R. Regalbuto, W.E. Mustain, High-performing commercial Fe-N-C cathode electrocatalyst for anion-exchange membrane fuel cells, *Nat. Energy* 6 (2021) 834–843, <https://doi.org/10.1038/s41560-021-00878-7>.
- S. Zhang, W. Yang, Y. Liang, X. Yang, M. Cao, R. Cao, Template-free synthesis of non-noble metal single-atom electrocatalyst with N-doped holey carbon matrix for highly efficient oxygen reduction reaction in zinc-air batteries, *Appl. Catal. B Environ.* 285 (2021), 119780, <https://doi.org/10.1016/j.apcatb.2020.119780>.
- H.W. Liang, W. Wei, Z.S. Wu, X. Feng, K. Mullen, Mesoporous metal-nitrogen-doped carbon electrocatalysts for highly efficient oxygen reduction reaction, *J. Am. Chem. Soc.* 135 (2013) 16002–16005, <https://doi.org/10.1021/ja407552k>.
- R. Li, Y. Li, P. Yang, D. Wang, H. Xu, B. Wang, F. Meng, J. Zhang, M. An, Electrodeposition: synthesis of advanced transition metal-based catalyst for hydrogen production via electrolysis of water, *J. Energy Chem.* 57 (2021) 547–566, <https://doi.org/10.1016/j.ijechem.2020.08.040>.
- X. Fu, G. Jiang, G. Wen, R. Gao, S. Li, M. Li, J. Zhu, Y. Zheng, Z. Li, Y. Hu, L. Yang, Z. Bai, A. Yu, Z. Chen, Densely accessible Fe-N<sub>x</sub> active sites decorated mesoporous carbon-spheres for oxygen reduction towards high performance aluminum-air flow batteries, *Appl. Catal. B Environ.* 293 (2021), 120176, <https://doi.org/10.1016/j.apcatb.2021.120176>.



- [31] J. Yang, W. Liu, M. Xu, X. Liu, H. Qi, L. Zhang, X. Yang, S. Niu, D. Zhou, Y. Liu, Y. Su, J.F. Li, Z.Q. Tian, W. Zhou, A. Wang, T. Zhang, Dynamic behavior of single-atom catalysts in electrocatalysis: identification of Cu-N<sub>3</sub> as an active site for the oxygen reduction reaction, *J. Am. Chem. Soc.* 143 (2021) 14530–14539, <https://doi.org/10.1021/jacs.1c03788>.
- [32] S. Li, C. Cheng, X. Zhao, J. Schmidt, A. Thomas, Active Salt/Silica-templated 2D mesoporous FeCo-Nx-carbon as bifunctional oxygen electrodes for zinc-air batteries, *Angew. Chem. Int. Ed. Engl.* 57 (2018) 1856–1862, <https://doi.org/10.1002/anie.201710852>.
- [33] M. Zhu, X. Zhao, X. Liu, X. Wang, F. Zhou, J. Wang, Y. Hu, Y. Zhao, T. Yao, L.-M. Yang, Y. Wu, Single atomic cerium sites with a high coordination number for efficient oxygen reduction in proton-exchange membrane fuel cells, *ACS Catal.* 11 (2021) 3923–3929, <https://doi.org/10.1021/acscatal.0c05503>.
- [34] X. Qu, Y. Han, Y. Chen, J. Lin, G. Li, J. Yang, Y. Jiang, S. Sun, Stepwise pyrolysis treatment as an efficient strategy to enhance the stability performance of Fe-Nx/C electrocatalyst towards oxygen reduction reaction and proton exchange membrane fuel cell, *Appl. Catal. B Environ.* 295 (2021), 120311, <https://doi.org/10.1016/j.apcatb.2021.120311>.
- [35] X. Wei, X. Luo, H. Wang, W. Gu, W. Cai, Y. Lin, C. Zhu, Highly-defective Fe-N-C catalysts towards pH-Universal oxygen reduction reaction, *Appl. Catal. B Environ.* 263 (2020), 118347, <https://doi.org/10.1016/j.apcatb.2019.118347>.
- [36] X. Yang, Y. Wang, G. Zhang, L. Du, L. Yang, M. Markiewicz, J.-Y. Choi, R. Chenitz, S. Sun, SiO<sub>2</sub>-Fe/N/C catalyst with enhanced mass transport in PEM fuel cells, *Appl. Catal. B Environ.* 264 (2020), 118523, <https://doi.org/10.1016/j.apcatb.2019.118523>.
- [37] L. Gong, H. Zhang, Y. Wang, E. Luo, K. Li, L. Gao, Y. Wang, Z. Wu, Z. Jin, J. Ge, Z. Jiang, C. Liu, W. Xing, Bridge bonded oxygen ligands between approximated FeN<sub>4</sub> sites confer catalysts with high ORR performance, *Angew. Chem. Int. Ed. Engl.* 59 (2020) 13923–13928, <https://doi.org/10.1002/anie.202004534>.
- [38] X. Lu, D. Wang, L. Ge, L. Xiao, H. Zhang, L. Liu, J. Zhang, M. An, P. Yang, Enriched graphitic N in nitrogen-doped graphene as a superior metal-free electrocatalyst for the oxygen reduction reaction, *New J. Chem.* 42 (2018) 19665–19670, <https://doi.org/10.1039/c8nj04857f>.
- [39] Y.-j. Wu, X.-h. Wu, T.-x. Tu, P.-f. Zhang, J.-t. Li, Y. Zhou, L. Huang, S.-g. Sun, Controlled synthesis of FeNx-CoNx dual active sites interfaced with metallic Co nanoparticles as bifunctional oxygen electrocatalysts for rechargeable Zn-air batteries, *Appl. Catal. B Environ.* 278 (2020), 119259, <https://doi.org/10.1016/j.apcatb.2020.119259>.
- [40] W. Zhu, Y. Pei, J.C. Douglin, J. Zhang, H. Zhao, J. Xue, Q. Wang, R. Li, Y. Qin, Y. Yin, D.R. Dekel, M.D. Guiver, Multi-scale study on bifunctional Co/Fe-N-C cathode catalyst layers with high active site density for the oxygen reduction reaction, *Appl. Catal. B Environ.* 299 (2021), 120656, <https://doi.org/10.1016/j.apcatb.2021.120656>.
- [41] X. Zhao, X. Li, Z. Bi, Y. Wang, H. Zhang, X. Zhou, Q. Wang, Y. Zhou, H. Wang, G. Hu, Boron modulating electronic structure of FeN<sub>4</sub>C to initiate high-efficiency oxygen reduction reaction and high-performance zinc-air battery, *J. Energy Chem.* 66 (2022) 514–524, <https://doi.org/10.1016/j.jechem.2021.08.067>.
- [42] X. Xu, Z. Xia, X. Zhang, R. Sun, X. Sun, H. Li, C. Wu, J. Wang, S. Wang, G. Sun, Atomically dispersed Fe-N-C derived from dual metal-organic frameworks as efficient oxygen reduction electrocatalysts in direct methanol fuel cells, *Appl. Catal. B Environ.* 259 (2019), 118042, <https://doi.org/10.1016/j.apcatb.2019.118042>.
- [43] X. Zhao, X. Yang, M. Wang, S. Hwang, S. Karakalos, M. Chen, Z. Qiao, L. Wang, B. Liu, Q. Ma, D.A. Cullen, D. Su, H. Yang, H.-Y. Zang, Z. Feng, G. Wu, Single-iron site catalysts with self-assembled dual-size architecture and hierarchical porosity for proton-exchange membrane fuel cells, *Appl. Catal. B Environ.* 279 (2020), 119400, <https://doi.org/10.1016/j.apcatb.2020.119400>.
- [44] H. Xu, D. Wang, P. Yang, L. Du, X. Lu, R. Li, L. Liu, J. Zhang, M. An, A hierarchically porous Fe-N-C synthesized by dual melt-salt-mediated template as advanced electrocatalyst for efficient oxygen reduction in zinc-air battery, *Appl. Catal. B Environ.* 305 (2022), 121040, <https://doi.org/10.1016/j.apcatb.2021.121040>.
- [45] R. Ma, G. Lin, Q. Ju, W. Tang, G. Chen, Z. Chen, Q. Liu, M. Yang, Y. Lu, J. Wang, Edge-sited Fe-N<sub>4</sub> atomic species improve oxygen reduction activity via boosting O<sub>2</sub> dissociation, *Appl. Catal. B Environ.* 265 (2020), 118593, <https://doi.org/10.1016/j.apcatb.2020.118593>.
- [46] Y.J. Sa, D.J. Seo, J. Woo, J.T. Lim, J.Y. Cheon, S.Y. Yang, J.M. Lee, D. Kang, T. J. Shin, H.S. Shin, H.Y. Jeong, C.S. Kim, M.G. Kim, T.Y. Kim, S.H. Joo, A general approach to preferential formation of active Fe-Nx Sites in Fe-N/C electrocatalysts for efficient oxygen reduction reaction, *J. Am. Chem. Soc.* 138 (2016) 15046–15056, <https://doi.org/10.1021/jacs.6b09470>.
- [47] S.H. Ahn, X. Yu, A. Manthiram, “Wiring” Fe-Nx-embedded porous carbon framework onto 1D nanotubes for efficient oxygen reduction reaction in alkaline and acidic media, *Adv. Mater.* 29 (2017) 1606534, <https://doi.org/10.1002/adma.201606534>.
- [48] Q. Wang, Y. Yang, F. Sun, G. Chen, J. Wang, L. Peng, W.T. Chen, L. Shang, J. Zhao, D. Sun-Waterhouse, T. Zhang, G.I.N. Waterhouse, Molten NaCl-assisted synthesis of porous Fe-N-C electrocatalysts with a high density of catalytically accessible FeN<sub>4</sub> active sites and outstanding oxygen reduction reaction performance, *Adv. Energy Mater.* 11 (2021) 2100219, <https://doi.org/10.1002/aenm.202100219>.
- [49] X. Jiang, J. Chen, F. Lyu, C. Cheng, Q. Zhong, X. Wang, A. Mahsud, L. Zhang, Q. Zhang, In situ surface-confined fabrication of single atomic Fe-N<sub>4</sub> on N-doped carbon nanoleaves for oxygen reduction reaction, *J. Energy Chem.* 59 (2021) 482–491, <https://doi.org/10.1016/j.jechem.2020.11.036>.
- [50] X. Li, Y. Zhao, Y. Yang, S. Gao, A universal strategy for carbon-based ORR-active electrocatalyst: one porogen, two pore-creating mechanisms, three pore types, *Nano Energy* 62 (2019) 628–637, <https://doi.org/10.1016/j.nanoen.2019.05.066>.
- [51] H. Xu, H. Jia, H. Li, J. Liu, X. Gao, J. Zhang, M. Liu, D. Sun, S. Chou, F. Fang, R. Wu, Dual carbon-hosted Co-N<sub>3</sub> enabling unusual reaction pathway for efficient oxygen reduction reaction, *Appl. Catal. B Environ.* 297 (2021), 120390, <https://doi.org/10.1016/j.apcatb.2021.120390>.